

Tailoring OAM spectrum of high-order harmonic generation driven by two mixed Laguerre-Gaussian beams with nonzero radial nodes

Beiyu Wang(汪倍羽), Jiaxin Han(韩嘉鑫), and Cheng Jin(金成)
Citation: Chin. Phys. B, 2023, 32 (**12**): 124208. DOI: 10.1088/1674-1056/ad0144
Journal homepage: http://cpb.iphy.ac.cn; http://iopscience.iop.org/cpb

What follows is a list of articles you may be interested in

Spectral shift of solid high-order harmonics from different channels in a combined laser field

Dong-Dong Cao(曹冬冬), Xue-Fei Pan(潘雪飞), Jun Zhang(张军), and Xue-Shen Liu(刘学深)
Chin. Phys. B, 2023, 32 (**3**): 034204. DOI: 10.1088/1674-1056/aca4bf

Effect of laser focus in two-color synthesized waveform on generation of soft x-ray high harmonics

Yanbo Chen(陈炎波), Baochang Li(李保昌), Xuhong Li(李胥红), Xiangyu Tang(唐翔宇), Chi Zhang(张弛), and Cheng Jin(金成)
Chin. Phys. B, 2023, 32 (**1**): 014203. DOI: 10.1088/1674-1056/ac8cea

Tunable spectral shift of high-order harmonic generation in atoms using a sinusoidally phase-modulated pulse

Yue Qiao(乔月), Jun Wang(王俊), Yan Yan(闫妍), Simeng Song(宋思蒙), Zhou Chen(陈洲), Aihua Liu(刘爱华), Jigen Chen(陈基根), Fuming Guo(郭福明), and Yujun Yang(杨玉军)
Chin. Phys. B, 2022, 31 (**6**): 064214. DOI: 10.1088/1674-1056/ac2d1c

Orientation and ellipticity dependence of high-order harmonic generation in nanowires

Fan Yang(杨帆), Yinghui Zheng(郑颖辉), Luyao Zhang(张路遥), Xiaochun Ge(葛晓春), and Zhinan Zeng(曾志男)
Chin. Phys. B, 2022, 31 (**4**): 044204. DOI: 10.1088/1674-1056/ac3ed0

A new method of calculating the orbital angular momentum spectra of Laguerre-Gaussian beams in channels with atmospheric turbulence

Xiao-zhou Cui(崔小舟), Xiao-li Yin(尹霄丽), Huan Chang(常欢), Zhi-chao Zhang(张志超), Yong-jun Wang(王拥军), Guo-hua Wu(吴国华)
Chin. Phys. B, 2017, 26 (**11**): 114207. DOI: 10.1088/1674-1056/26/11/114207

SPECIAL TOPIC — Optical field manipulation

Tailoring OAM spectrum of high-order harmonic generation driven by two mixed Laguerre–Gaussian beams with nonzero radial nodes

Beiyu Wang(汪倍羽)[1], Jiaxin Han(韩嘉鑫)[1], and Cheng Jin(金成)[1,2,†]

[1] *Department of Applied Physics, Nanjing University of Science and Technology, Nanjing* 210094, *China*

[2] *MIIT Key Laboratory of Semiconductor Microstructure and Quantum Sensing, Nanjing University of Science and Technology, Nanjing* 210094, *China*

(Received 4 July 2023; revised manuscript received 26 September 2023; accepted manuscript online 9 October 2023)

The extreme ultraviolet (XUV) light beam carrying orbital angular momentum (OAM) can be produced via high-order harmonic generation (HHG) due to the interaction of an intense vortex infrared laser and a gas medium. Here we show that the OAM spectrum of vortex HHG can be readily tailored by varying the radial node (from 0 to 2) in the driving laser consisting of two mixed Laguerre–Gaussian (LG) beams. We find that due to the change in spatial profile of HHG, the distribution range of the OAM spectrum can be broadened and its shape can be modified by increasing the radial node. We also show that the OAM mode range becomes much wider and its distribution shape becomes more symmetric when the harmonic order is increased from the plateau to the cutoff when the driving laser has the nonzero radial nodes. Through the map of coherence length and the evolution of harmonic field in the medium, we reveal that the favorable off-axis phase-matching conditions are greatly modified due to the change of intensity and phase distributions of driving laser with the radial node. We anticipate this work to stimulate some interests in generating the XUV vortex beam with tunable OAM spectrum through the gaseous HHG process achieved by manipulating the mode properties of the driving laser beam.

Keywords: orbital angular momentum (OAM) spectrum, high-order harmonic generation, Laguerre–Gaussian beam, radial nodes, phase-matching

PACS: 42.65.Ky, 42.65.Re, 78.47.jh, 42.65.–k **DOI:** 10.1088/1674-1056/ad0144

1. Introduction

An optical vortex refers to a light beam characterized by a helical phase structure, resulting in a spiral wavefront and the formation of a doughnut-shaped intensity distribution.[1–4] The presence of a phase singularity at the center of the beam defines its unique properties. Each photon in such a beam carries an orbital angular momentum (OAM) of $l\hbar$, where l is the topological charge, and $\hbar$ denotes the reduced Planck constant. The OAM associated with a vortex beam, also known as an OAM beam, can be transferred to atoms or molecules through the interaction between light and matter,[5–8] involving the exchange of momentum. The concept of the OAM beam was first demonstrated by Allen *et al*. in 1992 using a Laguerre–Gaussian (LG) beam.[9] The OAM beam provides an additional degree of freedom. With a unique OAM value (or single OAM mode), the vortex beam has been diversely applied in large-capacity communications,[10–13] gravitational wave detection,[14,15] optical tweezers and manipulation,[16,17] quantum information processing,[18,19] and other fields.[20–24]

It is important to note that a single vortex beam can also contain multiple OAM states, with the distribution of different OAM channels, known as the OAM spectrum, which greatly broadens its application areas. With a wide OAM spectrum, the vortex beam can be used in the ultrasensitive angular measurement,[25] the generation of arbitrary superpositions of atomic rotational states in a Bose–Einstein condensate,[26] the measurement of object parameters,[27] the performance of rotations and reflections on images,[28] and so on. To generate OAM spectra in the infrared (IR) and visible spectral ranges, there are several methods available including computer-generated holograms on the spatial light modulators,[29] specially designed metasurfaces,[30] integrated angular momentum gratings,[31,32] and coherent mixing of pre-generated vortex beams.[33] However, using optical elements is difficult to generate and tailor the OAM spectrum of light in the extreme ultraviolet (XUV) or soft x-rays.

One alternative approach is to utilize the high-order harmonic generation (HHG) resulting from the nonlinear interaction between an intense femtosecond IR laser and a gas medium.[34–41] This approach has been successfully employed to generate the vortex beam with high-value OAM in the XUV.[42,43] For example, Gairepy *et al*.[44] and Kong *et al*.[45] employed a noncollimated scheme by mixing two-color laser beams to control the OAM of HHG. Sanson *et al*.[46,47] conducted a measurement of HHG beams using an XUV Hartmann wave-front sensor, revealing the presence of multiple vortex modes. Rego *et al*.[48] theoretically investigated the generation of vortex HHG driven by non-pure LG modes and identified the nonperturbative characteristics of the OAM spectrum. Willi *et al*.[49] utilized two-color anti-spiral LG beams to generate HHG with specific OAM values, and they

†Corresponding author. E-mail: cjin@njust.edu.cn

© 2023 Chinese Physical Society and IOP Publishing Ltd

also coherently superimposed LG beams with different polarization states to generate the HHG and to control the OAM value.[50] Jin *et al.*[51] simulated the phase-matching conditions of HHG driven by a single LG beam with the nonzero OAM. Recently, Guan *et al.*[52] analyzed the macroscopic phase-matching mechanism for the OAM spectra of HHG by mixing two LG vortex modes and demonstrated that the OAM spectra can be readily tailored by varying the harmonic order, the position of the gas medium, and the energy ratio of two LG beams. Other aspects of OAM in the XUV through the HHG have also been intensively studied theoretically.[53–57] In these studies, the LG beam with zero radial node has been often used as the fundamental optical vortex. It is interesting to see how the vortex HHG can be changed by considering the nonzero radial nodes in the driving LG beam, especially the modification of the OAM spectrum.

Here our main goal is to identify how the radial node affects the OAM spectrum and the phase-matching condition of HHG driven by two mixed LG beams. Two LG modes are with equal wavelength and with topological charges of 1 and 2, and their radial nodes are simultaneously set as 0, 1, and 2, respectively. The article is arranged in the following. Section 2 will give a brief review of theoretical methods for simulating the vortex HHG, including the propagation equations of harmonic field, the formulation of far-field harmonic emissions, and the quantitative rescattering (QRS) model, and it will also present the comparison of spatial profiles and phase distributions of three mixed LG beams. In Section 3, we will show the spatial profiles of harmonics in the plateau and the cutoff, and will give the OAM spectra of far-field harmonics. We will reveal the phase matching of harmonics by employing two approaches. One is to calculate the coherence length through the phase mismatch between the driving laser and the high harmonic, and the other is to simulate the harmonic field in the gas medium by solving the three-dimensional Maxwell's wave equation. The conclusions will be presented in Section 4.

2. Theoretical methods

To simulate the vortex HHG driven by the mixed LG beams, we employ the general propagation theory in a gas medium, which has been established in Refs. [51,52]. Here we will only adopt some key equations, and will focus on the variation of spatial features of the mixed LG beams with the radial nodes.

2.1. Propagation equations of high-harmonic field in the gas medium

We assume that the fundamental LG beams carrying orbital angular momentum (OAM) remain unchanged while propagating through an ionized gas medium, resembling their behaviors in free space. The propagation characteristics of the vortex high-harmonic field in the ionizing medium can be described by (in a Cartesian coordinate)[51,52,58]

$$\nabla^2 E_{\rm h}(x,y,z,t) - \frac{1}{c^2}\frac{\partial^2 E_{\rm h}(x,y,z,t)}{\partial t^2} = \mu_0 \frac{\partial^2 P_{\rm nl}(x,y,z,t)}{\partial t^2}, \quad (1)$$

where

$$P_{\rm nl}(x,y,z,t) = [n_0 - n_{\rm e}(x,y,z,t)]D(x,y,z,t), \quad (2)$$

$$n_{\rm e}(t) = n_0\left\{1 - \exp\left[-\int_{-\infty}^{t} w(\tau)\,{\rm d}\tau\right]\right\}. \quad (3)$$

Here $P_{\rm nl}(x,y,z,t)$ is the nonlinear polarization, n_0 is the neutral atom density, $n_{\rm e}(x,y,z,t)$ is the free electron density, and $w(\tau)$ is the tunnel ionization rate. The induced dipole moment $D(x,y,z,t)$ is calculated in the local laser field. Effects of absorption and free electron dispersion are neglected.

2.2. Far-field harmonic emissions

Near-field harmonics are obtained from the exit face of a gas medium ($z_{\rm out}$). After a long distance propagation in vacuum, they reach the detector and are called far-field harmonics, which can be obtained in the frequency domain by using Huygens' integral under the paraxial and Fresnel approximations (in a Cartesian coordinate) as[51,52,59]

$$E_{\rm h}^{\rm f}(x_{\rm f},y_{\rm f},z_{\rm f},\omega) = \frac{{\rm i}k}{2\pi L}\int\int \tilde{E}_{\rm h}(x,y,z_{\rm out},\omega) \times \exp\left\{-\frac{{\rm i}k}{2L}\left[(x_{\rm f}-x)^2 + (y_{\rm f}-y)^2\right]\right\}{\rm d}x{\rm d}y. \quad (4)$$

Here $L = z_{\rm f} - z_{\rm out}$, $z_{\rm f}$ is the far-field position from laser focus, $x_{\rm f}$ and $y_{\rm f}$ are the transverse coordinates in the far field, and the wave vector k is given by $k = \omega/c$. Note that Eq. (4) is used to calculate the harmonic field on a plane at $z_{\rm f}$ perpendicular to the propagation axis, while far-field harmonics are computed in a spherical surface with a radius L.

2.3. Quantitative rescattering model for single-atom response

Single-atom induced dipole moment, denoted as $D(t)$ in Eq. (3), can be accurately calculated by using the quantitative rescattering (QRS) model.[60,61] In this model, $D(t)$ is expressed in the frequency domain as $D(\omega)$, which can be written as[58]

$$D(\omega) = \sqrt{N}W(\omega)d(\omega). \quad (5)$$

Here N represents the ionization probability taken at the end of the laser pulse, $d(\omega)$ corresponds to the complex photorecombination (PR) transition dipole matrix element, and $W(\omega)$ is the complex microscopic wave packet. The QRS model improves the strong-field approximation (SFA) by using a more accurate scattering wave in the calculation of the PR transition dipole, instead of using a simple plane wave in the SFA.[62] However, the returning wave packet remains the

same as that used in the SFA. In practice, the QRS obtains the accurate induced dipole moment as[60,61]

$$D^{\rm qrs}(\omega) = D^{\rm sfa}(\omega)\sqrt{\frac{N^{\rm qrs}}{N^{\rm sfa}}\frac{d^{\rm qrs}(\omega)}{d^{\rm sfa}(\omega)}}, \tag{6}$$

where both $D^{\rm sfa}(\omega)$ and $d^{\rm qrs}(\omega)$ are complex numbers, while $d^{\rm sfa}(\omega)$ is either a pure real or pure imaginary number. $N^{\rm qrs}$ is calculated by the ADK theory.[63]

2.4. Fundamental Laguerre–Gaussian beams

Under the paraxial and slowly varying transverse amplitude approximations, the electric field of the Laguerre–Gaussian (LG) beam can be expressed in a cylindrical coordinates as[51,52,59]

$$\begin{aligned}&{\rm LG}_{l,p}(r,\phi,z')\\ &= E_0\frac{w_0}{w(z')}\left(\frac{r}{w(z')}\right)^{|l|}L_p^{|l|}\left(\frac{2r^2}{w^2(z')}\right)\exp\left(-\frac{r^2}{w^2(z')}\right)\\ &\times\exp\left(-{\rm i}k_0\frac{r^2}{2R(z')}-{\rm i}\zeta(z')-{\rm i}l\phi\right).\end{aligned} \tag{7}$$

Note that the expression provided above is written in the moving frame ($z'=z$, $t'=t-z/c$), and therefore, the factor of $\exp(-{\rm i}k_0 z)$ in the rest frame has been omitted. w_0 represents the beam waist at the focus, $w(z')=w_0\sqrt{1+(z'/z_0)^2}$ is the beam width, with $z_0=\pi w_0^2/\lambda_0$ being the Raylaigh length at laser wavelength λ_0. $L_p^{|l|}$ is the associated Laguerre polynomial, $R(z')=z'[1+(z_0/z')^2]$ is the curvature radius of the wave front, and the Gouy phase is given by $\zeta(z')=-(|l|+2p+1)\arctan(z'/z_0)$. Here l takes values of $\pm0,1,2,\ldots$, representing the topological charge, while p takes values of $\pm0,1,2,\ldots$, associated with the number of radial nodes.

For the driving laser, we consider coherently mixing two LG vortex modes with topological charges of $l_1=1$ and $l_2=2$, and their numbers of radial node are chosen as $p_1=p_2=0$, 1, and 2 in three sets, respectively. Laser wavelength is fixed at 800 nm. To ensure a significant overlap between two beams in each set, we choose beam waists at the focus of 25 μm for $l_1=1$ and 17.7 μm for $l_2=2$ such that the maximum intensity appears in the same radial distance for $p_1=p_2=0$. These parameters are maintained for $p_1=p_2\neq0$ even though it is not possible to achieve complete spatial overlap of two beams. To balance the energy distribution, we adjust the amplitudes of E_0 so that the energies of two beams are always equal in three sets. By coherently combining the two beams, we obtain a maximum laser intensity of 2.5×10^{14} W/cm^2 at the focus. This intensity is sufficiently high to drive the high-order harmonic generation (HHG) process with argon gas.

In Fig. 1, we illustrate the intensity and phase distributions of three mixed LG beams. Note that near-field results are shown using the real size of the driving laser beam around the laser focus while far-field ones are displayed in terms of the divergence angle to eliminate the dependence on the propagation distance. In the near field, for $p_1=p_2=0$, the intensity distribution exhibits a single revolving and half-ring structure in Fig. 1(a). Unlike the single-valued OAM beam, the cylindrical symmetry in the intensity distribution is no longer exited. The phase is not evenly changed with the azimuthal angle in Fig. 1(d). With the increase of radial nodes, additional revolving ring structures appear in the intensity distribution beyond the half-ring with maximum intensity, resulting in a total of $p+1$ rings, see Figs. 1(b) and 1(c). As p increases, the radius of the half-ring with the maximum intensity decreases and the radius of outmost intensity ring increases. The phase changes in multiple incomplete rings, and there exhibits the phase shift between two neighboring rings, see Figs. 1(e) and 1(f). In the far field, three mixed beams display the same number of intensity rings as that in the near field, and the ring with maximum intensity remains the most inner one in Figs. 1(g)–1(i). The phase distributions of the three cases are quite different as shown in Figs. 1(j)–1(l). The shape of phase distribution varies dramatically from $p=0$ to $p=2$ due to the Gouy phase $\zeta(z')$. Note that from $z'=0$ to $z'=+\infty$, the phase shift is $-\pi$ ($-3/2\pi$), -2π ($-5/2\pi$), or -3π ($-7/2\pi$) for ${\rm LG}_{1,0}$ (${\rm LG}_{2,0}$), ${\rm LG}_{1,1}$ (${\rm LG}_{2,1}$), or ${\rm LG}_{1,2}$ (${\rm LG}_{2,2}$) mode, respectively. Thus, mixing two LG beams results in the complicated Gouy phase shift in the far field.

3. Results and discussion

3.1. Comparison of spatial profiles and OAM spectra of H13 generated by mixed two LG beams

In the simulations, we employ a Gaussian envelope to model the temporal profile of the laser pulse. The pulse has a full-width-at-half-maximum (FWHM) duration of 10 optical cycles (or 26.7 fs) at 800 nm and the carrier-envelope-phase (CEP) of 0. The temporal waveform and laser wavelength are kept the same for all LG beams. The spatial part is obtained by coherently combining two LG beams as shown in Fig. 1. A 1 mm long Ar gas jet with uniform density distribution is applied and its center is located at 1.5 mm after laser focus.

For three sets of mixed LG beams, we show the intensity distributions of 13th-order harmonic (H13) after propagation in the medium (near field, at exit face of gas jet) and in vacuum (far field, far away from gas jet) in Fig. 2. In the near field, first, harmonic emissions are mostly distributed on the right half plane for ${\rm LG}_{1,0}+{\rm LG}_{2,0}$ in Fig. 2(a), and on the left half plane for ${\rm LG}_{1,1}+{\rm LG}_{2,1}$ and ${\rm LG}_{1,2}+{\rm LG}_{2,2}$ in Figs. 2(b) and 2(c). Second, the distribution of harmonic intensity is centered between about 20 μm to 40 μm and its radius gets smaller and smaller when p is increased from 0 to 2. These areas of harmonic emissions are consistent with ring regions having the maximum intensity of driving laser in Figs. 1(a)–1(c). In the far field, intensity distribution of H13 by ${\rm LG}_{1,0}+{\rm LG}_{2,0}$ remains a single half-ring structure in Fig. 2(d), but multiple rings appear in the emission distribution in Fig. 2(e) when p is increased to 1. In Fig. 2(f), when $p=2$, the multiple ring structure is quite different from that in Fig. 2(e).

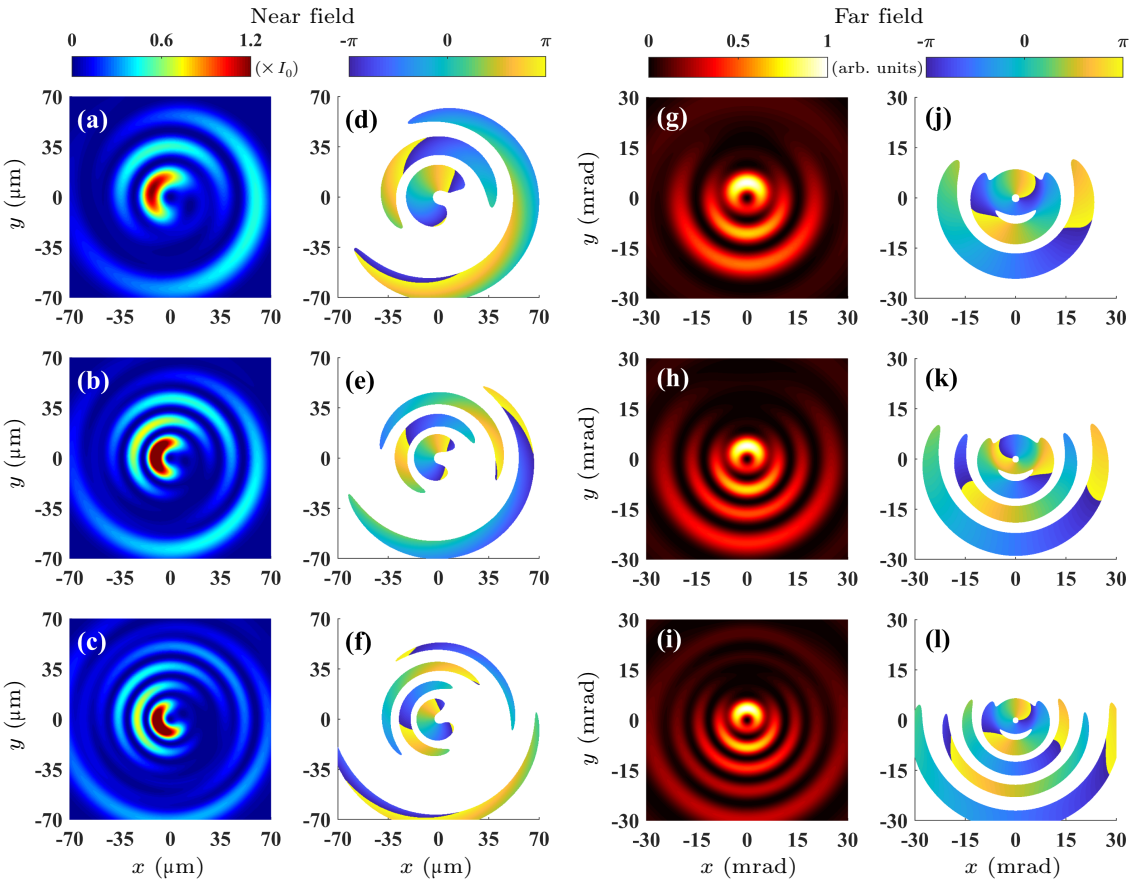


Fig. 1. Transverse intensity and phase profiles of mixed LG beams in the near field ($z' = 1.5$ mm, left) and in the far field ($z' = +\infty$, right). First row: $\mathrm{LG}_{1,0} + \mathrm{LG}_{2,0}$; second row: $\mathrm{LG}_{1,1} + \mathrm{LG}_{2,1}$; third row: $\mathrm{LG}_{1,2} + \mathrm{LG}_{2,2}$. The phase is defined from $-\pi$ to π, and $I_0 = 10^{14}$ W/cm^2.

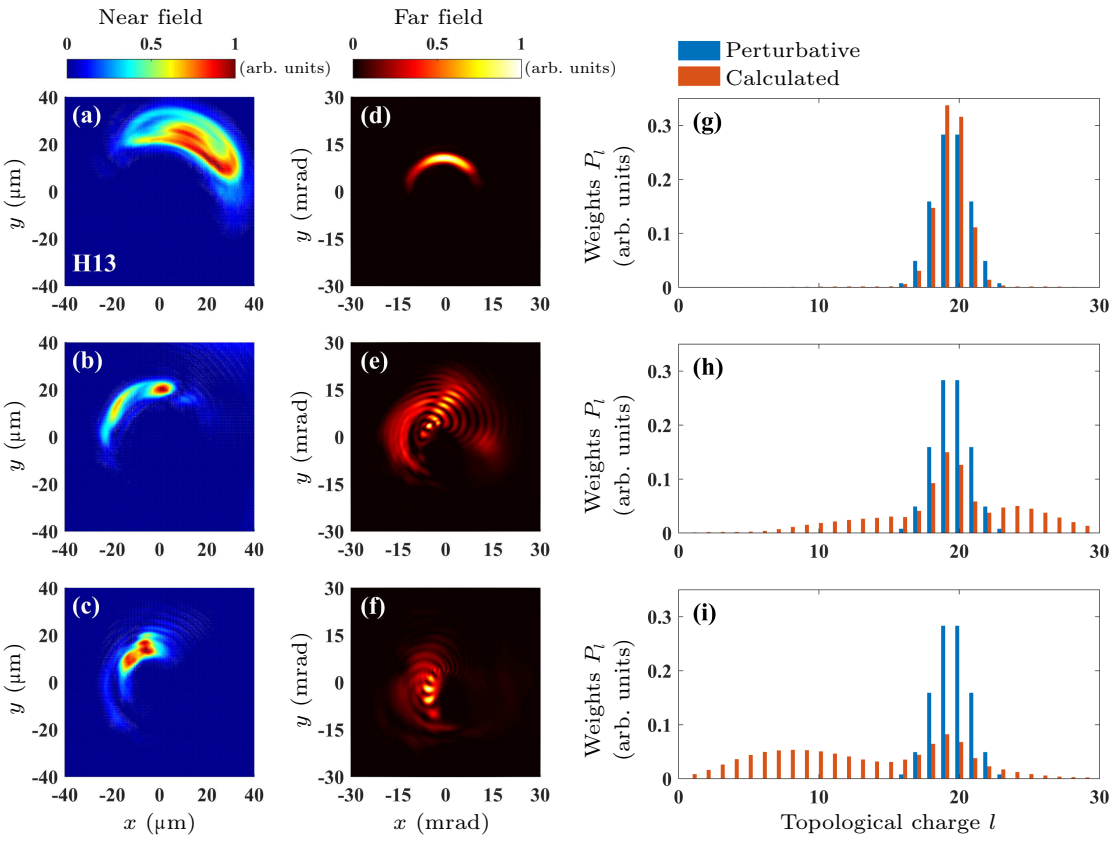


Fig. 2. Spatial intensity profiles of H13 in the near field (left column) and in the far field (middle column) driven by three sets of mixed LG beams. OAM spectra are calculated by using far-field harmonic fields and given by the perturbative theory (right column). First row: $\mathrm{LG}_{1,0} + \mathrm{LG}_{2,0}$; second row: $\mathrm{LG}_{1,1} + \mathrm{LG}_{2,1}$; third row: $\mathrm{LG}_{1,2} + \mathrm{LG}_{2,2}$.

We next decompose the far-field harmonic to calculate the contribution of different OAM modes. The complex electric field of far-field harmonic is expressed as $E_{\rm far}(\omega, r_{\rm far}, \phi)$, in which the z coordinate is omitted. We perform the azimuthal Fourier transform along the azimuthal coordinate ϕ in the following:[52,64,65]

$$c_l(\omega, r_{\rm far}) = \frac{1}{2\pi}\int_0^{2\pi} E_{\rm far}(\omega, r_{\rm far}, \phi)\, {\rm e}^{{\rm i}l\phi}\, {\rm d}\phi, \tag{8}$$

where l is the topological charge of OAM mode, and the normalized weight of each mode is obtained by the integration along $r_{\rm far}$ as

$$P_l(\omega) = \frac{\int_0^{\infty} |c_l(\omega, r_{\rm far})|^2 r_{\rm far}\, {\rm d}r_{\rm far}}{\sum_l \int_0^{\infty} |c_l(\omega, r_{\rm far})|^2 r_{\rm far}\, {\rm d}r_{\rm far}}. \tag{9}$$

For comparison, we also evaluate the OAM spectrum of HHG in the perturbative regime. To simplify the analysis, we focus solely on the azimuthal-angle dependence in the LG beam. The electric field of LG beam can be expressed as $E_{1,p} = E_1\, {\rm e}^{{\rm i}l_1\phi}$ (or $E_{2,p} = E_1\, {\rm e}^{{\rm i}l_2\phi}$) with the complex amplitude $E_{i=1,2}$ and the topological charge $l_{i=1,2}$. For the perturbative harmonic, its electric field $E_{\rm h}(\omega)$ is proportional to the q-th power of the driving laser field as[52]

$$\begin{aligned} & E_{\rm h}(\omega) \propto (E_{1,0} + E_{2,0})^q \\ = & \ (E_1\, {\rm e}^{{\rm i}l_1\phi} + E_2\, {\rm e}^{{\rm i}l_2\phi})^q \\ = & \sum_{n=0}^{q} \frac{q!}{(q-n)!n!} E_1^{q-n} E_2^n\, {\rm e}^{{\rm i}[(q-n)l_1 + nl_2]\phi}, \end{aligned} \tag{10}$$

and the normalized weight for the OAM mode with topological charge $l = (q-n)l_1 + nl_2$ is obtained as

$$P_l(\omega) = \frac{\left|\frac{q!}{(q-n)!n!} E_1^{q-n} E_2^n\right|^2}{\sum_{n=0}^{q} \left|\frac{q!}{(q-n)!n!} E_1^{q-n} E_2^n\right|^2}, \tag{11}$$

where $\omega = q\omega_0$ with the fundamental frequency ω_0.

The calculated OAM spectra with far-field harmonic fields (including the phase, not shown) and perturbative OAM spectrum for H13 are both plotted in Figs. 2(g)–2(i). One can see that the calculated OAM spectrum is greatly tailored by varying the radial node in the driving laser. In comparison with the perturbative OAM spectrum, the calculated one is similar to it in both the spectral range and the peak OAM mode when $p = 0$, see Fig. 2(g). But the calculated OAM spectra have broader ranges in Figs. 2(h) and 2(i) when the radial node is increased to 1 or 2. They have the same OAM peak at $l = 19$. In addition, the OAM spectrum of $p = 2$ has an extra peak structure around $l = 8$. This indicates that the radial node in the driving laser can not only broaden the OAM spectrum of HHG but also change its shape.

3.2. Analysis of phase-matching mechanism of H13 driven by different mixed LG beams

We then employ two approaches to uncover the origins of the change of high harmonics with the radial node in the driving laser, i.e., coherence length analysis and numerical simulations based on Maxwell's wave equations. The second approach can be performed by solving the propagation equations of the high-harmonic field in Eq. (1). Two methods allow us to examine the phase-matching conditions and the accumulation of harmonic strength within the gas medium. For a given azimuthal angle of 90°, intensity distributions of mixed LG laser beams, maps of the coherence length of H13, and the evolution of harmonic field in the medium are plotted in the z–r plane in Fig. 3.

Let us introduce the first approach in detail. The total wave vector $\boldsymbol{k}_1$ for the fundamental mixed LG beam can be expressed as[51]

$$\boldsymbol{k}_1(r, \phi, z) = k_0 \boldsymbol{e}_z - \nabla\varphi(r, \phi, z), \tag{12}$$

where $\boldsymbol{e}_z$ is the unit vector along the z direction, $k_0 = \omega_0/c$ with the laser frequency ω_0, and $\varphi(r, \phi, z)$ is the geometric phase of the mixed LG beam. The effective wave vector $\boldsymbol{K}$ to describe the spatial dependence of atomic phase in the single-atom response is

$$\boldsymbol{K}(r, \phi, z) = \nabla\Phi_{q,{\rm dip}}(r, \phi, z). \tag{13}$$

Here $\Phi_{q,{\rm dip}}(r, \phi, z)$ is the intrinsic dipole phase, which can be written as

$$\Phi_{q,{\rm dip}}(r, \phi, z) = -\alpha_i^q I(r, \phi, z), \tag{14}$$

where $I(r, \phi, z)$ represents the laser pear intensity at a given spatial position of the mixed LG beam. Note that unlike the single-mode LG beam, the intensity distribution of the mixed LG beam does not exhibit azimuthal-angle symmetry. The coefficients α_i^q depend on the short (S) or long (L) trajectory and the harmonic order. For harmonics in the plateau, $\alpha^q_{i={\rm S}} \approx 1\times10^{-14}$ rad·cm^2·W^{-1} and $\alpha^q_{i={\rm L}} \approx 24\times10^{-14}$ rad·cm^2·W^{-1}. At the cutoff, $\alpha^q_{i={\rm S,L}} \approx 13.7\times10^{-14}$ rad·cm^2·W^{-1},[51] where two trajectories are merged into one.[66,67] The mismatch of wave vectors between the q-th harmonic and the fundamental laser can be defined as $\delta k_q(r, \phi, z)$, its direction is along the polarization wave vector $q\boldsymbol{k}_1 + \boldsymbol{K}$, and thus its norm is[51]

$$\delta k_q(r, \phi, z) = k_q - |q\boldsymbol{k}_1 + \boldsymbol{K}|, \tag{15}$$

with $k_q = q\omega_0/c$. Finally the coherence length can be introduced as

$$L_{q,{\rm coh}}(r, \phi, z) = \frac{\pi}{|\delta k_q(r, \phi, z)|}. \tag{16}$$

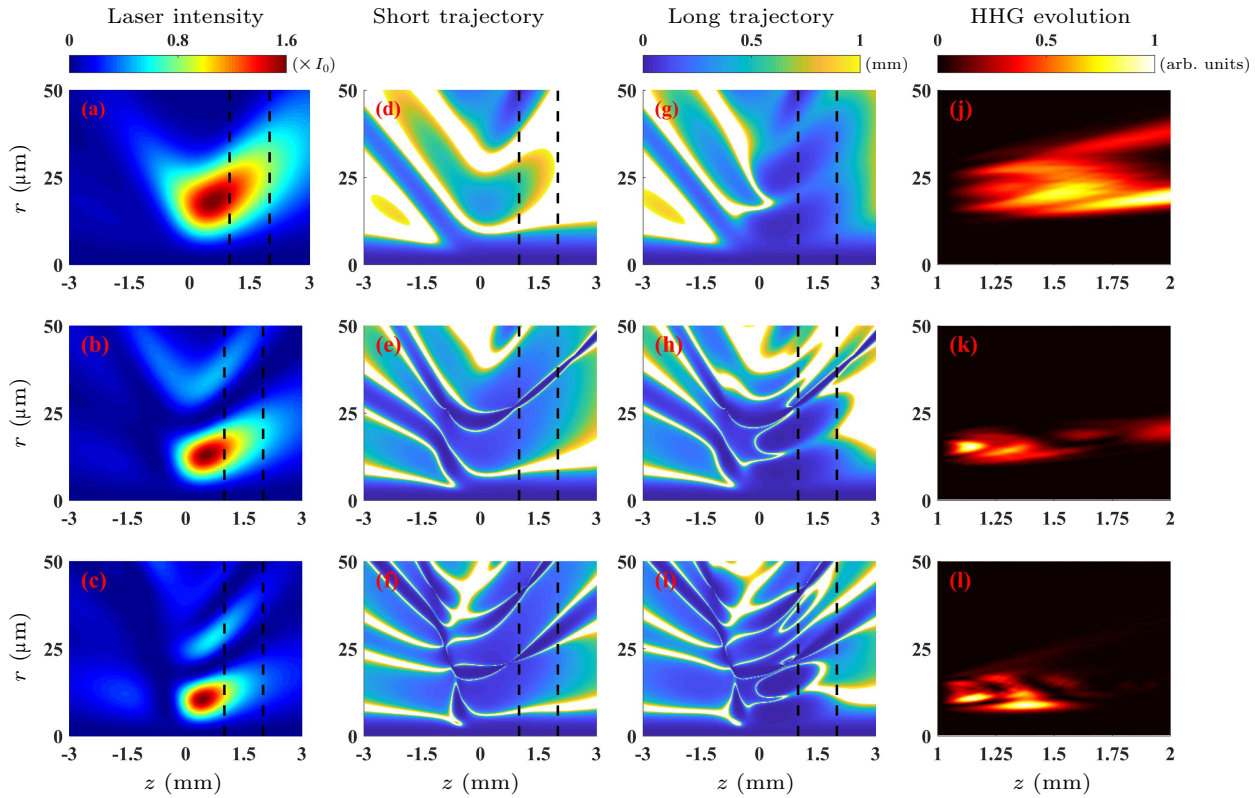


Fig. 3. Laser intensity distributions of three mixed LG beams (left column), maps of the coherence length of H13 due to short and long trajectories, respectively (two middle columns), and the evolution of harmonic field in the medium (right column). Results are shown for a fixed azimuthal angle of 90°. First row: $LG_{1,0}+LG_{2,0}$; second row: $LG_{1,1}+LG_{2,1}$; third row: $LG_{1,2}+LG_{2,2}$. Note that the white color indicates that the coherence length is longer than 1 mm. The area between two dashed lines specifies the position of the gas medium and $I_0 = 10^{14}$ W/cm^2.

We show the calculated spatial coherence length in the z–r plane for H13 in Figs. 3(d)–3(f) and 3(g)–3(i) by only considering harmonic emissions from either short or long trajectories. The intrinsic phase accumulated by an electron following the short or long trajectory is quite different, resulting in two distinct maps of harmonic coherence length. Spatial intensity profiles of mixed LG beams are also plotted in Figs. 3(a)–3(c) for easily identifying effective phase-matching regions. These figures can help understand the spatial distributions of near-field harmonics in Fig. 2. For example, in Fig. 3(a), the laser intensity around $r = 20$ μm is decreased within the gas medium along the propagation axis (labeled by two dashed lines). In the same spatial areas in Figs. 3(d) and 3(g), the phase-matching regions for the short trajectory, indicated by the white color, are much better compared to that for the long trajectory, which is predominantly represented by blue color. The favorable phase-matching condition for the short trajectory leads to the gradual growth of the harmonic field, as depicted in Fig. 3(j), especially after $z = 1.5$ mm. By increasing the radial node, one can observe the significant difference in the map of coherence length. For $p = 1$, considering the spatial area of effective intensity distribution of driving laser, the phase-matching region of short trajectory around $r = 12$ μm starts from a narrow one at $z = 0$ mm and becomes broader along the propagation axis in Fig. 3(e), while the long trajectory exhibits very poor phase-matching in the same area in Fig. 3(h). Due to the interference of harmonic emissions from both trajectories, the harmonic field cannot continuously grow up within the 1-mm-long gas medium in Fig. 3(k). Furthermore, even though the phase-matching condition of short trajectory for $p = 2$ appears similar to that for $p = 1$, see the comparison of Figs. 3(e) and 3(f), the harmonic field only constantly grows before $z = 1.5$ mm in Fig. 3(l). This is because the white area in Fig. 3(f) is narrower than that in Fig. 3(e), meanwhile the length of white area of long trajectory in Fig. 3(i) is much shorter than the length of gas medium, which is not enough for accumulating harmonic yields. Thus, the phase-matching condition of the harmonic is greatly modified by varying the radial node in the mixed LG beam, leading to a significant difference in the spatial harmonic profile in the near field in Fig. 2.

3.3. Comparison of emission properties of H29 in the cutoff generated by different mixed LG beams

For the harmonics in the cutoff, we choose H29 as a representative for presentation and analysis. Its spatial profiles in both near and far fields are plotted in Fig. 4 together with its far-field OAM spectra. It is evident that intensity structures are much cleaner compared to results for H13, particularly for $p = 1$ and 2 in Figs. 4(b) and 4(c). Furthermore, regardless of the p values, all the distributions of harmonic emissions exhibit a single half-ring structure in both near and far fields.

For the OAM spectra, the calculated ones remain broader than the perturbative ones for three cases. And they also show a symmetrical distribution, unlike that of H13. When $p = 0$, the peak of the calculated OAM spectrum is the same as that of perturbative one, see Fig. 4(g). And its peak is shifted by increasing the radial node as shown in Figs. 4(h) and 4(i). Thus in the cutoff, the clean spatial profile (including the phase) of harmonic leads to the broad and symmetrical distribution of the OAM spectrum regardless of radial node in the driving laser.

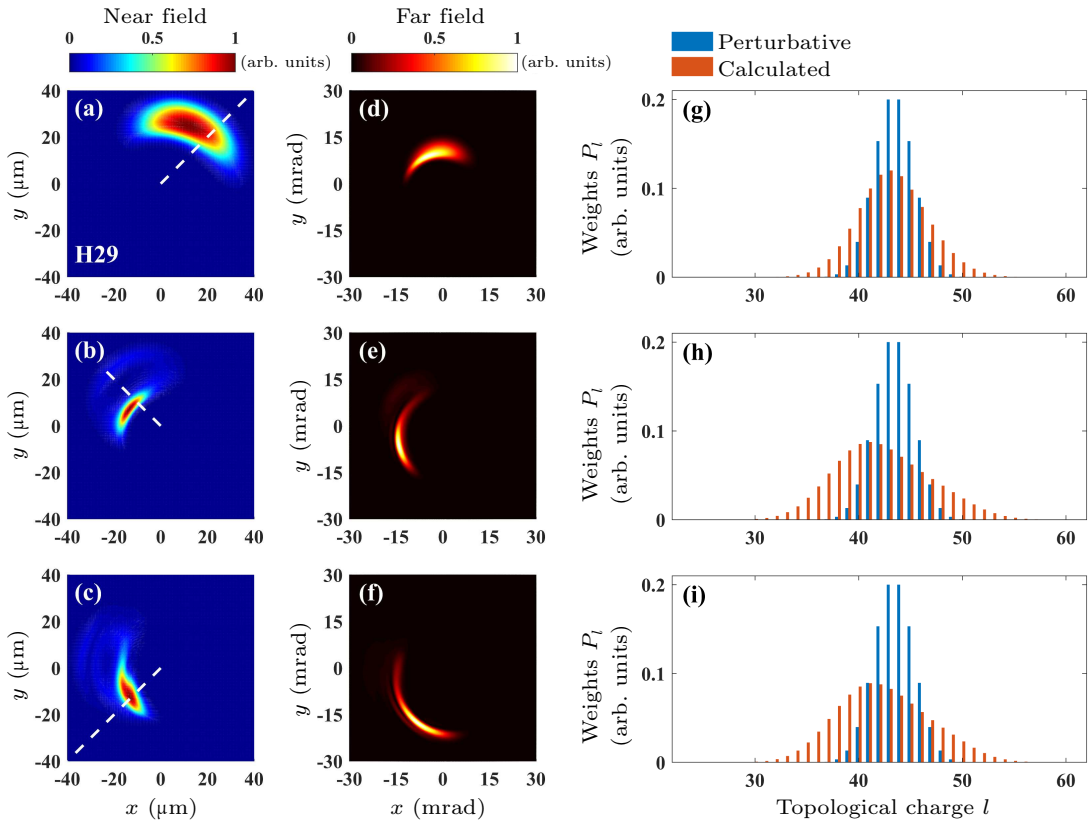


Fig. 4. Same as Fig. 2 but for H29. Dashed lines indicate different azimuthal angles used in Fig. 5.

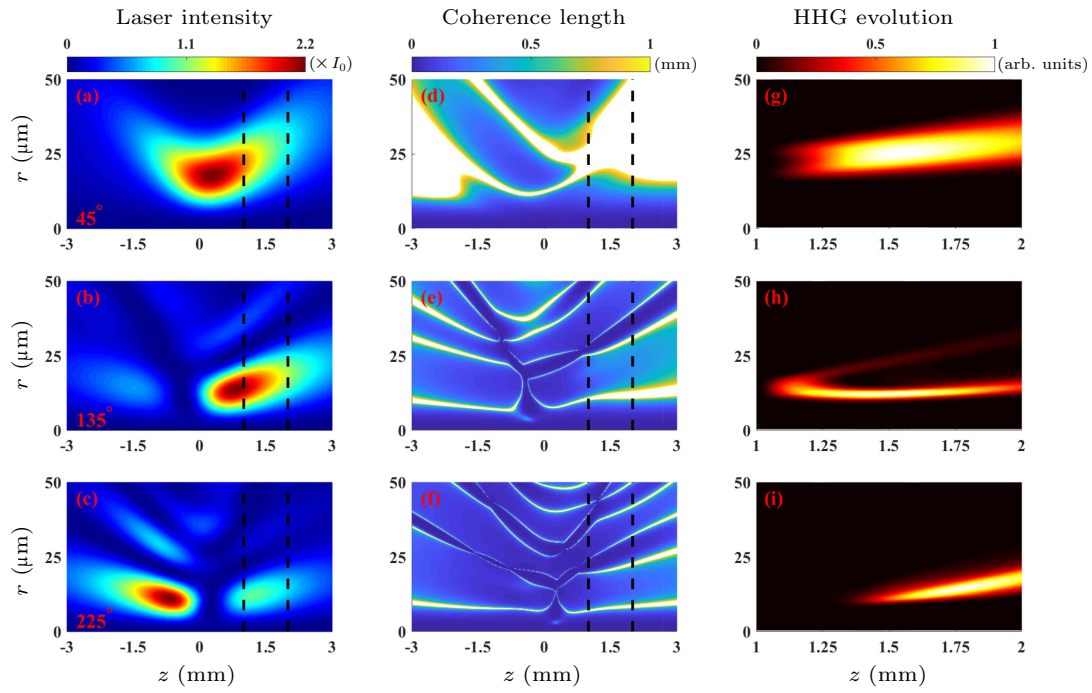


Fig. 5. Similar figure to Fig. 3 except for H29. Note that maps of coherence length (middle column) for cutoff harmonic are plotted where short and long trajectories are merged. Azimuthal angle is 45°, 135°, and 225° in the first, second, and third rows, respectively.

To understand the presence of the single caritive-ring structure in the spatial profile in the near field, we analyze the phase-matching conditions of cutoff harmonic H29, where the short and long trajectories are coming together. In Fig. 5 we choose different azimuthal angles for three mixed LG beams, which are plotted in Figs. 4(a)–4(c) by dashed lines, thus for $p = 2$, the peak intensity of driving laser appears at $z < 0$ mm. Considering the area of effective intensity distribution, a quite broad white color region occurs off axis when $p = 0$ in Fig. 5(d), explaining the growth of the harmonic field in a wide radial range in Fig. 5(g). When p increases, the phase-matching area around $r = 10$ μm becomes narrower in Figs. 5(e) and 5(f), implying that the harmonic field can only be accumulated within a limited region. In Figs. 5(h) and 5(i), the evolution of the harmonic field develops in a long and slender shape, which is consistent with the phase-matching picture. Therefore, the single caritive-ring structure exhibiting in the spatial profile of near-field harmonic is due to the good (or limited) phase-matching achieved off axis for cutoff harmonic. Since high harmonics in the plateau and cutoff regions are generated from different electron trajectories, their phase-matching conditions are quite different as shown in Figs. 3 and 5. Thus the behavior of the OAM spectrum in the far field exhibits a strong dependence on the harmonic order.

3.4. Illustration of harmonic vortex features for selected high harmonics in the plateau

We finally show the spatial profiles in the far field and the corresponding OAM spectra in Fig. 6 for another two harmonics in the plateau, i.e., H15 and H21. In the case of $p = 0$, the spatial distribution of harmonic intensity keeps the single half-ring structure, see Figs. 6(a) and 6(b). Thus the calculated OAM spectrum resembles the perturbative one as shown in Figs. 6(c) and 6(d). In addition, the OAM spectrum becomes broader as the harmonic order increases. For $p = 1$, as shown in Figs. 6(e) and 6(f), the multiple-ring structure appears in the spatial profile, and the number of ring decreases with the increase of harmonic order. Taking into account of results for H13 and H29, we can conclude that the multiple-ring structure occurring in the presence of radial node in the driving laser can be gradually eliminated by increasing the harmonic order. The OAM spectrum can maintain a reasonably well symmetric distribution, see Figs. 6(g) and 6(h). When $p = 2$, the harmonic intensity has a similar multiple-ring structure to that for $p = 1$, but its distribution is more irregular, as shown in Figs. 6(i) and 6(j), leading to the asymmetrical OAM spectral distribution in Figs. 6(k) and 6(l). For example, in Fig. 6(k), there is a noticeable increase in the weight of OAM mode, which is developed on the left side of peak one, determined by the perturbative theory. So the OAM spectrum can also be readily tailored with the harmonic order. This is valid even though considering the radial node in the driving laser.

Note that we have performed simulations for vortex high harmonics driven by the mixed LG beams with higher radial nodes, specifically with $p = 3$ and 4. We have checked that for both plateau and cutoff harmonics, the spanning range of the OAM spectrum and its shape do not change much when the

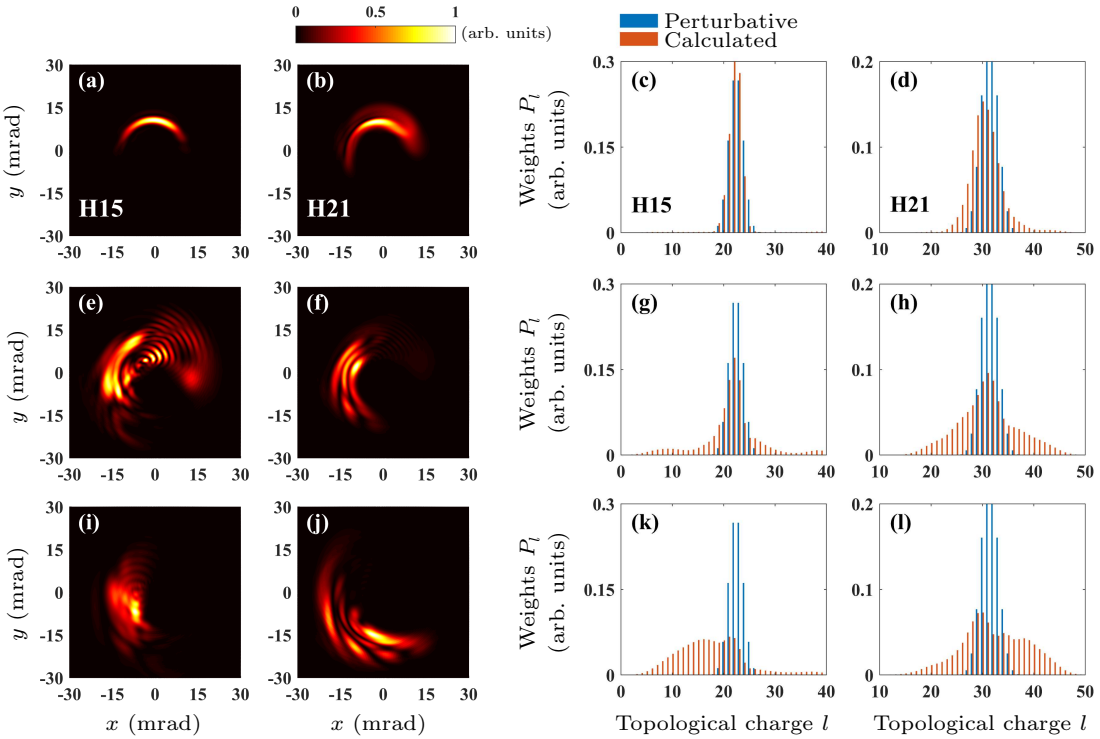


Fig. 6. Intensity profiles of H15 (first column) and H21 (second column) in the far field and corresponding OAM spectra (third and fourth columns). First row: $LG_{1,0} + LG_{2,0}$; second row: $LG_{1,1} + LG_{2,1}$; third row: $LG_{1,2} + LG_{2,2}$.

radial node is increased from 2 to 4. This is because when the radial node is set as 3 or 4 the mixed LG beams show a similar ring with the maximum intensity around the laser focus to that when the radial node is 2. This intensity ring contributes mostly to the generation of vortex HHG. This also indicates that effective tailoring of the OAM spectrum of HHG by varying the radial node is limited in the range of 0 to 2.

4. Conclusion

We proposed to effectively modify the orbital angular momentum (OAM) spectrum of vortex HHG by varying the radial node in the two mixed LG beams. Our investigation was based on the well-established and rigorous approach for simulating the vortex HHG from the gas medium, i.e., solving the Maxwell's wave equation of harmonic field in the medium, computing the single-atom response with the QRS model, and projecting the near-field harmonic to the far field using Huygens' integral. We found that by increasing the radial node (from 0 to 2) in the driving laser the single half-ring structure in the spatial profile switches to the multiple caritive-ring structure for high harmonics at the plateau. For high harmonics at the cutoff, the single half-ring structure appearing in the spatial profile for $p = 0$ does not change with the radial node. We showed that by varying the radial node, the OAM spectrum of far-field harmonic can change its shape and broaden its distribution region. For a given radial node of 1 or 2, with the increase of harmonic order, the mode range of the OAM spectrum becomes wider and wider, and its distribution tends to be more symmetric. We adopted two methods to uncover the phase-matching mechanism of high harmonics in the plateau and the cutoff, i.e., analyzing the spatial map of coherence length and the evolution of harmonic field in the medium. By varying the radial node, the spatial intensity and phase distributions of mixed two LG beams are greatly changed, leading to the difference in the favorable phase-matching regions off axis, which is consistent with the growth of harmonic field in the medium.

This work offers a practical way to tailor the OAM spectra of high-order harmonics in the XUV by modifying the properties of driving LG beams. Meanwhile it further strengthens our standing of the phase-matching nature of vortex HHG driven by nonpure OAM modes with radial nodes.

Acknowledgments

Project supported by the National Natural Science Foundation of China (Grant Nos. 12274230, 91950102, and 11834004) and the Funding of Nanjing University of Science and Technology (Grant No. TSXK2022D005).

References

[1] Shen Y J, Wang X J, Xie Z W, Min C J, Fu X, Liu Q, Gong M L and Yuan X C 2019 *Light: Sci. Appl.* **8** 90
[2] Omatsu T, Miyamoto K and Lee A J 2017 *J. Opt.* **19** 123002
[3] Yao A M and Padgett M J 2011 *Adv. Opt. Photonics* **3** 161
[4] Padgett M J and Miles J 2017 *Opt. Express* **25** 11265
[5] Picón A, Benseny A, Mompart J, Vázquez de Aldana J R, Plaja L, Calvo G F and Roso L 2010 *New J. Phys.* **12** 083053
[6] Alexandrescu A, Cojoc D and Di Fabrizio E 2006 *Phys. Rev. Lett.* **96** 243001
[7] Babiker M, Bennett C R, Andrews D L and Dávila Romero L C 2002 *Phys. Rev. Lett.* **89** 143601
[8] Giri S, Ivanov M and Dixit G 2020 *Phys. Rev. A* **101** 033412
[9] Allen L, Beijersbergen M W, Spreeuw R J C and Woerdman J P 1992 *Phys. Rev. A* **45** 8185
[10] Wang J, Yang J Y, Fazal I M, Ahmed N, Yan Y, Huang H, Ren Y X, Yue Y, Dolinar S, Tur M and Willne A E 2012 *Nat. Photonics* **6** 488
[11] Bozinovic N, Yue Y, Ren Y X, Tur M, Kristensen P, Huang H, Willner A E and Ramachandran S 2013 *Science* **340** 1545
[12] Lei T, Zhang M, Li Y, Jia P, Liu G N, Xu X, Li Z, Min C, Lin J, Yu C, Niu H and Yuan X 2015 *Light: Sci. Appl.* **4** e257
[13] Fu S Y, Zhai Y W, Zhou H, Zhang J Q, Wang T L, Yin C and Gao C Q 2019 *Opt. Lett.* **44** 4753
[14] Granata M, Buy C, Ward R and Barsuglia M 2010 *Phys. Rev. Lett.* **105** 231102
[15] Andreas N, Christina B and Benno W 2017 *Opt. Lett.* **42** 751
[16] Padgett M J and Bowman R W 2011 *Nat. Photonics* **5** 343
[17] Yang Y J, Ren Y X, Chen M Z, Arita Y and Rosales-Guzmán C 2021 *Adv. Photonics* **3** 034001
[18] Götte J B, O'Holleran K, Preece D, Flossmann F and Padgett M J 2008 *Opt. Express* **16** 993
[19] Mafu M, Dudley A, Goyal S K, Giovannini D, Mclaren M, Padgett M J, Konrad T, Petruccione F, Lütkenhaus N and Forbes A 2013 *Phys. Rev. A* **88** 032305
[20] Lavery M P J, Speirits F C, Barnett S M and Padgett M J 2013 *Science* **341** 537
[21] Fu S Y, Wang T L, Zhang Z Y, Zhai Y W and Gao C Q 2017 *Opt. Express* **25** 20098
[22] Belmonte A, Rosales-Guzmán C and Torres J P 2015 *Optica* **2** 1002
[23] Páez-López R, Ruiz U, Arrizon V and Ramos-Garcia R 2016 *Opt. Lett.* **41** 4138
[24] Tao S H, Yuan X C and Lin J 2005 *Opt. Express* **13** 7726
[25] D'Ambrosio V, Spagnolo N, Del Re L, Slussarenko S, Li Y, Kwek L C, Marrucci L, Walborn S P, Aolita L and Sciarrino F 2013 *Nat. Commun.* **4** 2432
[26] Andersen M F, Ryu C, Cladé P, Natarajan V, Vaziri A, Helmerson K and Phillips W D 2006 *Phys. Rev. Lett.* **97** 170406
[27] Xie G D, Song H Q, Zhao Z, Milione G and Willner A E 2017 *Opt. Lett.* **42** 4482
[28] Li F S, Xu T Z, Zhang W H, Qiu X D, Lu X C and Chen L X 2018 *Appl. Phys. Lett.* **113** 161109
[29] Zhu L and Wang J 2015 *Opt. Express* **23** 26221
[30] Chen S M, Yuan C, Li G X, Zhang S and Cheah K W 2016 *Laser Photonics Rev.* **10** 322
[31] Xiao Q X, Klitis C, Li S M, Chen Y Y, Cai X L, Sorel M and Yu S Y 2016 *Opt. Express* **24** 3168
[32] Li H L, Strain M J, Meriggi L, Chen L F, Zhu J B, Cicek K, Wang J W, Cai X L, Sorel M, Thompson G M and Yu S Y 2015 *Appl. Phys. Lett.* **107** 051102
[33] Kapale K T and Dowling J P 2005 *Phys. Rev. Lett.* **95** 173601
[34] Li X F, L'Huillier A, Ferray M, Lompré L A and Mainfray G 1989 *Phys. Rev. A* **39** 5751
[35] Hoflund M, Peschel J, Plach M, Dacasa H, Veyrinas K, Constant E, Smorenburg P, Wikmark H, Maclot S, Guo C, Arnold C, L'Huillier A and Eng-Johnsson P 2021 *Ultrafast Sci.* **2021** 9797453
[36] Lang Y, Peng Z and Zhao Z 2022 *Chin. Phys. Lett.* **39** 114201
[37] Guo X L, Jin C, He Z, Zhao S F, Zhou X X and Cheng Y 2021 *Chin. Phys. Lett.* **38** 123301
[38] Zhang H, Liu X, Jin F, Zhu M, Yang S, Dong W, Song X and Yang W 2021 *Chin. Phys. Lett.* **38** 063201
[39] Wang S, Guo J, He X, Liang Y, Xie B, Zhong S, Teng H and Wei Z 2023 *Chin. Phys. B* **32** 063301
[40] Xing Y H, Zhang J, Huo X X, Xu Q Y and Liu X S 2022 *Chin. Phys. B* **31** 043203

[41] He L X, Zhu X S, Cao W, Lan P F and Lu P X 2022 *Chin. Phys. B* **31** 123301
[42] Rego L, Dorney K M, Brooks N J, Nguyen Q L, Liao C T, Román J S, Couch D E, Liu A, Pisanty E, Lewenstein M, Plaja L, Kapteyn H C, Murnane M M and Hernández-García C 2019 *Science* **364** eaaw9486
[43] Hernádez-García C, Vieira J, Mendona J T, Rego L, Román J S, Plaja L, Ribič P R, Gauthier D and Picón A 2017 *Photonics* **4** 28
[44] Gauthier D, Ribič P R, Adhikary G, Camper A, Chappuis C, Cucini R, DiMauro L F, Dovillaire G, Frassetto F, Géneaux R, Miotti P, Poletto L, Ressel B, Spezzani C, Stupar M, Ruchon T and Ninno G D 2017 *Nat. Commun.* **8** 14971
[45] Kong F, Zhang C, Bouchard F, Li Z, Brown G G, Ko D H, Hammond T J, Arissian L, Boyd R W, Karimi E and Corkum P B 2017 *Nat. Commun.* **8** 14970
[46] Sanson F, Pandey A K, Harms F, Dovillaire G, Baynard E, Demailly J, Guilbaud O, Lucas B, Neveu O, Pittman M, Ros D, Richardson M, Johnson E, Li W, Balcou P and Kazamias S 2018 *Opt. Lett.* **43** 2780
[47] Sanson F, Pandey A K, Papagiannouli I, Harms F, Dovillaire G, Baynard E, Demailly J, Guilbaud O, Lucas B, Neveu O, Pittman M, Ros D, Richardson M, Johnson E, Li W, Balcou P and Kazamias S 2020 *Opt. Lett.* **45** 4790
[48] Rego L, Román J S, Picón A, Picon L and Hernández-García C 2016 *Phys. Rev. Lett.* **117** 163202
[49] Paufler W, Böing B and Fritzsche S 2019 *J. Opt.* **21** 094001
[50] Paufler W, Böing B and Fritzsche S 2019 *Phys. Rev. A* **100** 013422
[51] Jin C, Li B C, Wang K, Xu C H and Lin C D 2020 *Phys. Rev. A* **102** 033113
[52] Guan Z, Yin Z M and Jin C 2022 *Phys. Rev. A* **105** 023107
[53] Hernádez-García C, Picón A, Román J S and Plaja L 2013 *Phys. Rev. Lett.* **111** 083602
[54] Hernádez-García C, Román J S, Plaja L and Picón A 2015 *New J. Phys.* **17** 093029
[55] Telnov D A and Chu S I 2017 *Phys. Rev. A* **96** 033807
[56] Paufler W, Böing B and Fritzsche S 2018 *Phys. Rev. A* **98** 011401
[57] Wang Z, Hong W Y, Wang F and Liao Q 2020 *Phys. Rev. Res.* **2** 033482
[58] Abro N, Wang K, Zhu X H, Li B C and Jin C 2018 *Phys. Rev. A* **98** 023411
[59] Han J, Tang X, Yin Z, Wang K, Fu Y, Wang B, Chen Y, Zhang C and Jin C 2022 *Opt. Express* **30** 47942
[60] Le A T, Lucchese R R, Tonzani S, Morishita T and Lin C D 2009 *Phys. Rev. A* **80** 013401
[61] Lin C D, Le A T, Jin C and Wei H 2018 *J. Phys. B* **51** 104001
[62] Lewenstein M, Balcou P, Ivanov M Y, L'Huillier A and Corkum P B 1994 *Phys. Rev. A* **49** 2117
[63] Jin C, Le A T, Trallero-Herrero C A and Lin C D 2011 *Phys. Rev. A* **84** 043411
[64] D'Errico A, D'Amelio R, Piccirillo B, Cardano F and Marrucci L 2017 *Optica* **4** 1350
[65] Zhang L G, Shen B F, Bu Z G, Zhang X M, Ji L L, Huang S, Xiriai M, Xu Z L, Liu C and Xu Z Z 2021 *Phys. Rev. Appl.* **16** 014065
[66] Lewenstein M, Salières P and L'Huillier A 1995 *Phys. Rev. A* **52** 4747
[67] Gaarde M B and Schafer K J 2002 *Phys. Rev. A* **65** 031406